Highly stable Pt/CoAl$_2$O$_4$ catalysts in Aqueous-Phase Reforming of glycerol

A.J. Reynoso [a], U. Iriarte-Velasco [b], M.A. Gutiérrez-Ortiz [a], J.L. Ayastuy [a, *]

[a] A.J. Reynoso, M.A. Gutiérrez-Ortiz, J.L. Ayastuy

Chemical Technologies for the Environmental Sustainability Group

Department of Chemical Engineering, Faculty of Science and Technology

University of the Basque Country UPV/EHU, Sarriena S/N, 48940 Leioa, Spain

Corresponding author: joseluis.ayastuy@ehu.eus

[b] U. Iriarte-Velasco

Chemical Technologies for the Environmental Sustainability Group

Department of Chemical Engineering, Faculty of Pharmacy

University of the Basque Country UPV/EHU,

Paseo de la Universidad, 7, 01006 Vitoria, Spain

Abstract

Pt/CoAl$_2$O$_4$ catalysts with small amounts of Pt (0.3 and 1 wt.%) were prepared by wet impregnation of platinum on cobalt aluminate (mole ratio Co/Al=0.625). These catalysts were compared with monometallic Pt/alumina and cobalt aluminate counterparts. The physicochemical characteristics of the obtained materials were thoroughly analysed. The catalytic performance of the prepared assays was investigated in the Aqueous-Phase Reforming (APR) of glycerol for up to 100 h TOS, and in liquid phase Water-Gas Shift (WGS). It was concluded that the addition of Pt to cobalt aluminate resulted in a synergistic effect that promoted the reduction of both Pt and Co species, as well as cobalt dispersion, what increased the amount of exposed metallic sites. These effects were, however, sensitive to the amount of Pt loaded. The glycerol APR activity of bimetallic catalysts was very stable over 100 h TOS with conversion values above 99%. Conversion to gas was also above 95% during the whole operation. Contrarily, the counterpart monometallic catalysts suffered noticeable deactivation at above 70 h TOS. Also, WGS activity of bimetallic assays was higher than the monometallic counterparts. Addition of Pt to cobalt aluminate lowered selectivity to hydrogen, due to a higher CO hydrogenation activity. Examination of the spent catalysts showed better textural stability of the bimetallic samples, as well as much lesser formation of carbonaceous surface deposits. Nevertheless, oxidation and leaching of cobalt remains as the main drawback of bimetallic catalysts to be used in APR.

1. Introduction

The environmental concern related to the use of fossil fuels has driven much interest in renewable energy production from biomass. In particular, glycerol is an inexpensive and readily available sub-product of biodiesel units that can be used to produce hydrogen [1]. Due to its high functionalization, glycerol presents high chemical reactivity that allows its valorisation by, among other routes, oxidation, reforming, hydrodeoxygenation, and hydrogenation [2].

Hydrogen produced from biomass is an alternative to traditional fossil feedstocks and can be therefore part of a low-carbon energy system. Aqueous-Phase Reforming (APR) is one of the most straightforward methods for the valorisation of glycerol which enables the production of hydrogen or alkanes by tuning the catalysts properties and operation conditions [3] (Figure 1). APR can be used for a sort of oxygenated substrates, as oxygenated hydrocarbons feedstock from biomass (sugars and polyols), Fisher-Tropsch residuals [4] or food industry residuals [5,6]. The APR process is advantageous over conventional steam reforming, since it works at lower temperatures and somewhat higher pressures, which eliminates the necessity to vaporize the feedstream, with the energy-saving advantage thereof. Typically, APR process is conducted in the 220-260 ºC range and at moderate pressure (30-50 bar) in order to keep the reaction mixture in liquid phase. In addition, this low working temperatures shift the WGS equilibrium, so an hydrogen stream with low CO concentration can be obtained in a single reactor.

APR of an oxygenated hydrocarbon proceeds through a complex reaction network, and ideally, results in H_2 and CO_2 mixture. In the case of glycerol APR over transition metal catalysts, two main paths have been proposed [7] (Figure 1): through Path I, promoted by metallic sites, hydroxyl group at primary carbon is dehydrogenated to give glyceraldehyde, which rapidly undergoes C-C scission resulting in ethylene glycol and CO. Ethylene glycol undergoes further dehydrogenation and C-C cleavage, while CO can react via Water-Gas Shift giving additional hydrogen [8]. WGS is considered the rate-limiting step in APR [9].
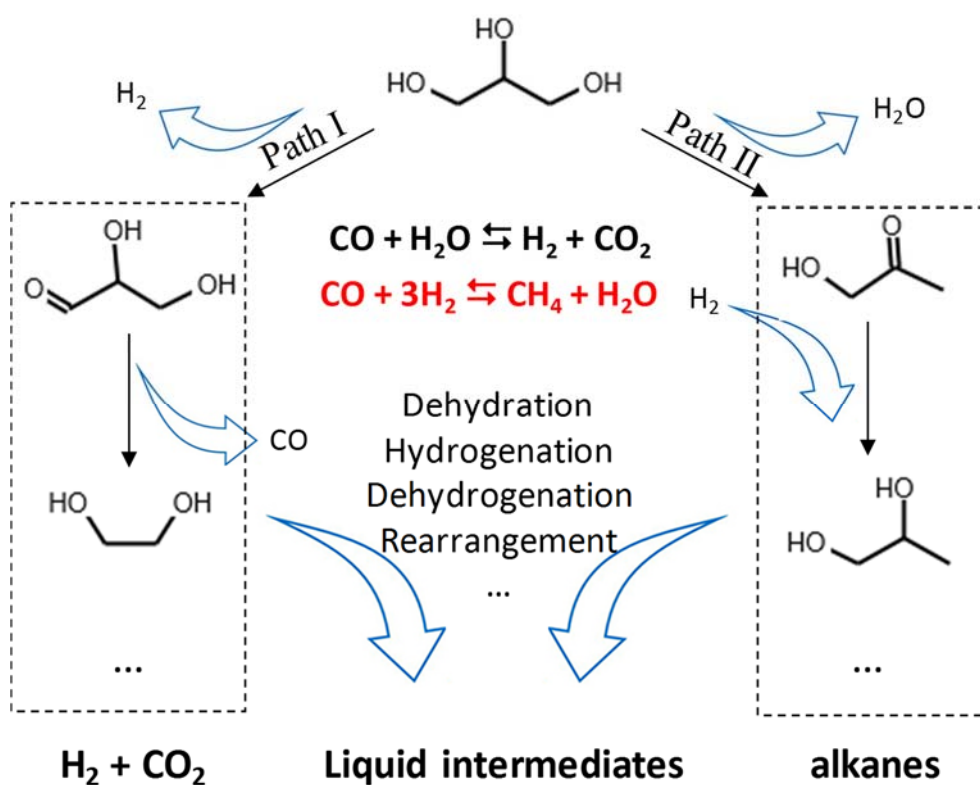
Figure 1. Main reaction paths in glycerol APR (adapted from [7]).

Overall, the glycerol APR (reaction 1) gives, ideally, 7 moles of hydrogen per mole of converted glycerol.

$$C_3H_8O_3 \text{ (l)} + 3H_2O \text{ (l)} \rightarrow 7H_2 + 3CO_2 \qquad \Delta H^0 = +348.1 \text{ kJ/mol} \qquad (1)$$

Through Path II, glycerol is firstly dehydrated to hydroxyacetone, which subsequently can be hydrogenated to propylene glycol. The resulting intermediates are further converted through a complex reaction system that involves hydrogenation/dehydrogenation/dehydration/hydrogenolysis reactions. Path II is promoted by acidic supports, which enables high yields to alkanes, as well as intermediate liquid oxygenates. In order to maximize hydrogen yield, Path I should be favoured, what would require mainly metallic sites in the catalyst. Thus, an effective catalyst should be active for C-C and C-H bond cleavage, as well as for WGS reaction [10], which is a key reaction to convert to CO_2 the primary product CO from decarbonylation, and simultaneously produce additional hydrogen. In addition, in order to achieve high hydrogen yield, catalyst should be inactive in C-O bond cleavage and avoid hydrogen consumption in parallel hydrogenation reactions, which give rise to light alkanes and liquid intermediates [11]. Among the suitable metals for APR, Pt has outstanding performance due to its high C-C scission and WGS activity. However, transition metals such as Ni or Co have been also investigated [12,13]. Metal combinations of Pt, Co and others have been proposed in order to enhance the catalyst performance in many reactions [14-16]. Dietrich et al. [11] reported that the

addition of Co to Pt (molar ratio 1:1) increased glycerol conversion, H_2 and CO_2 production by a factor of 2 for the APR of glycerol. Dosso et al. [17] showed a beneficial effect upon addition of Ni or Co to Pt catalysts, evidenced as an increase in the yield to hydrogen, improved stability, and lessening of coke deposits.

APR is performed under harsh hydrothermal conditions, therefore, catalyst deactivation is commonly an issue. The main causes vary depending on the active metal, the support and the type of reactor used [18]. Active metal leaching (especially transition metals) [19-21] and/or oxidation and deposition of graphitic carbon [22] have been reported as main causes.

In our previous work [7] we prepared cobalt aluminate spinel derived catalysts for APR of glycerol with relatively high Co dispersion. The most active assay (bulk Co/Al molar ratio of 0.625) converted 88% of glycerol with 22% conversion to gas, at 235 ºC/3.5 MPa, and produced 231 $\mu mol_{H2}/g_{cat} \cdot min$, with 60% H_2 in the gas stream. However, catalyst stability was compromised. In order to solve this aspect and enhance the space-time yields, in this work different amounts of platinum were impregnated on cobalt aluminate. The catalytic performance was tested in the Aqueous-Phase Reforming of 10 wt.% glycerol/water synthetic mixtures, and the obtained results discussed in terms of the structure-activity-stability relationship. For comparison, 0.3Pt/γ-alumina and bare cobalt aluminate samples were also tested.

2. Experimental Section

2.1. Catalysts preparation

Cobalt aluminate spinel (nominal Co/Al mole ratio=0.625) was prepared by coprecipitation, as reported elsewhere [7]. Briefly, proper amounts of aqueous solutions of cobalt(II) nitrate hexahydrate and aluminium(III) nitrate nonahydrate were coprecipitated with sodium carbonate at pH 10. The resulting suspension was aged at room temperature for 24 h, filtered, washed several times with de-ionized water, dried at 110 ºC for 17 h and calcined in a muffle furnace at 500 ºC (heating rate 5 ºC/min) for 5 h in a static air atmosphere. This sample was abbreviated CoAl.

Platinum (with nominal contents of 0.3 and 1 wt.%) was added to the cobalt aluminate spinel (CoAl) by wet impregnation method, using tetraammineplatinum(II) nitrate (Alfa Aesar, % 99.99) as the metal precursor, dissolved in deionized water. After impregnation, the solids were dried at 110 ºC for 17 h and finally, calcined in air at 350 ºC in a muffle furnace (heating rate 5 ºC/min) for 3 h. These samples were abbreviated xPt/CoAl, where x denotes the nominal wt.% of Pt. For comparative purposes, γ-Al_2O_3-supported Pt catalyst was prepared by the same procedure (abbreviated 0.3Pt/Al). γ-alumina was prepared by calcination of aluminium(III) nitrate nonahydrate in air, at 500 ºC for 4 h (heating rate 5 ºC/min).

2.2. Catalysts characterization

ICP-AES (Perkin Elmer, Optima 8300) was used to analyse the metal concentration in the prepared catalysts and also in the liquid phase products. Prior to analysis, solid samples were digested in *aqua regia* (volume ratio HCl/HNO$_3$: 3/1) in closed containers for 24 h at 100 ºC. Reaction exhaust liquid samples were previously diluted in nitric acid (ratio 1:50). Textural properties of the solids were measured by nitrogen adsorption-desorption isotherms at 77 K, carried out into Micromeritics TriStar II 3020 apparatus. Prior to the adsorption, samples were outgassed at 300 ºC for 10 h. Specific surface area was calculated by BET method, while the pore size distribution was determined with BJH formalism. The crystalline structure of the samples was analysed by XRD (PANalytical X´pert PRO diffractometer, using CuKα radiation, λ=1.5406 Å). Each sample was scanned from 10 to 90° (2θ), with a step size of 0.026° (2θ) and a counting time of 2 s. Phase identification was done by comparison of the obtained spectra and the PDF database. Scherrer equation was used to calculate the crystallite average size.

^{27}Al Solid State NMR measurements were performed on a 9.4 T Bruker AVANCE III 400 spectrometer operating at resonance frequencies of 104.26 MHz for ^{27}Al. Chemical shifts were referenced externally to the AlCl$_3$ aqueous solution at 0 ppm. The spectra were acquired at a spinning frequency of 60 kHz employing a PH MASDVT400W BL 1.3mm ultrafast probe head. A single pulse of 0.3 microseconds duration was applied and a recycle delay of 0.2 s and 36,000 scans were used.

Temperature programmed reduction (H$_2$-TPR) was carried out using an Micromeritics AutoChem 2920 apparatus, equipped with thermal conductivity detector (TCD). About 50 mg of sample was heated in He stream at 500 °C for 1 h (heating rate 10 °C/min) to clean the sample. Then, the temperature was lowered to ambient temperature into Ar flow. Finally, in 5% H$_2$-Ar flow, the temperature was ramped to 950 ºC at 10 ºC/min heating rate, and hold for 1 h.

H$_2$ chemisorption was carried out in a Micromeritics AutoChem 2920 equipment in dynamic mode, at 40 ºC. Discrimination between Pt and Co metallic sites, was effected by applying two consecutive chemisorption pulses. Previously, surface was cleaned into He flow at 500 ºC. First, catalysts was reduced at 250 ºC in 5%H$_2$/Ar flow (heating rate 10 ºC/min, hold 1 h), and cooled down to 40 ºC in Ar flow. Pulses of 5%H$_2$/Ar were injected (loop volume 0.5312 mL) until peaks had equal area. Secondly, the sample was heated in 5%H$_2$/Ar flow to 600 ºC (heating rate 10 ºC/min, hold 1 h), and evacuated in Ar for 15 min. Temperature was cooled down to 40 ºC into Ar flow and a new pulse chemisorption was completed. Hydrogen uptake by the sample reduced at 250 ºC was assigned to Pt sites, while uptake after reduction at 600 ºC was assigned to both Pt and Co sites. H/Me (Me=Pt, Co) stoichiometry of 1/1 was assumed.

Total surface acidity was measured by weighing the chemisorbed ammonia by thermogravimetry (Setaram Setsys). About 80 mg of sample was placed in an alumina crucible, and in-situ reduced at 600 ºC for 2 h under 50 mL/min 5%H_2/Ar flow. The sample was then cooled down to 50 ºC under 50 mL/min 5%H_2/Ar flow. Thereafter, the flow was switched to 10%NH_3/He (16 mL/min) for 1 h. Finally, the ammonia flow was stopped while 5%H_2/Ar (50 mL/min) was circulated through the reactor for 1 h in order to desorb the physisorbed ammonia. The eventual mass gain of the sample corresponded to the chemisorbed ammonia.

X-ray photoelectron spectroscopy (XPS) was used to detect the electronic state of Pt, Co and Al in the prepared samples. The spectra were measured using a SPECS spectrometer with Phoibos 150 1DDLD analyser and monochromatized Al Kα (1486.7 eV) X-ray radiation in ultrahigh vacuum. Binding energies were calibrated by taking C 1s peak (284.6 eV) of adventitious carbon as reference. The peaks were deconvoluted after Shirley background subtraction, using a mixed Gaussian-Lorentzian function and concentrations were calculated by correcting the values with relative atomic sensitivity factors (Scofield).

Raman analysis of the spent catalysts was carried out in a Renishaw InVia Raman spectrometer coupled to a Leica DMLM microscope, using a laser of 514 nm (ion-argon laser, Modu-Laser). The power density of the laser beam was reduced in order to avoid the photo-decomposition of the samples. In order to improve the signal to noise ratio, 40 s were used for each spectrum and 10 scans were accumulated at 10% of the maximum power of the 514 nm laser, in the 1000-2000 cm^{-1} spectral window.

Deposition of carbonaceous material on the spent catalysts was quantified by Temperature Programmed Hydrogenation (TPH) in a Micromeritics AutoChem 2920 coupled to a Mass Spectrometer (Pffeifer Vacuum OmniStar). Sample was first heated at 550 °C for 1 h, under a He flow, and cooled down to ambient temperature. Then, a flow of 5%H_2/Ar was passed through the sample heated at 10 °C/min up to 950 ºC and m/z=15 (CH_4) signal was recorded.

Nitrogen isotherms and XRD were carried out for samples reduced ex-situ in a tubular quartz reactor at 600 ºC for 1 h (heating rate 5 ºC/min) in 50% H_2-He flow (50 mL/min).

2.3. Catalytic test

The APR test of 10 wt.% glycerol in water (glycerol/water mole ratio 0.0217) synthetic mixture was carried out in a fixed-bed up-flow reactor (internal diameter=5.1 mm; length=305 mm) made in Hastelloy (Microactivity Effi, PID Eng&Tech). About 1.8 g of catalyst (particle size 0.04-0.16 mm) was placed on a stainless steel frit, covered with a quartz wool plug, and then reduced under 10 %H_2/He flow at 600 ºC for 2 h (heating rate 5 ºC/min) at atmospheric pressure. The reactor was

pressurised with He up to the desired pressure, then the He flow was switched to bypass and 0.02 mL/min of the liquid feedstream (pH 6.6) pumped into the reactor while the temperature was progressively raised at 5 ºC/min up to the reaction temperature. Catalytic tests were carried out at 260 ºC and 50 bar at a WHSV of 0.68 h^{-1} (calculated as feed mass flow/catalyst mass) with a total duration of 100 h. Zero time was taken when reactants reached the catalyst bed, once ensured the reaction temperature was reached. The reaction products were cooled down to 5 ºC and the gas and liquid phases separated. The gas phase was passed through 100 mL mixing vessel in order to minimize the pulses of gas products coming from the reactor, and analysed online every 30 min by a gas chromatograph (µGC Agilent), equipped with four parallel columns. The liquid fraction was manually collected in 3 mL vials every 1 h, and then off-line analysed by either gas chromatography (GC-FID Agilent, HP-WAX) and HPLC (Waters 616, Hi-Plex H column) equipped with Refraction Index Detector. The total organic carbon (TOC) was measured off-line on a Shimadzu TOC-L apparatus. Details about the gas and liquid product external calibration curves are given in the Supporting Information file.

The total glycerol conversion (X_{Gly}), the carbon conversion to gas (X_{gas}), hydrogen selectivity (S_{H2}), hydrogen yield (Y_{H2}), alkane selectivity ($S_{alkanes}$) and liquid products yield (Y_i) were calculated as follows:

$$X_{Gly}(\%) = 100 \times \frac{F_{Gly}^{in} - F_{Gly}^{out}}{F_{Gly}^{in}} \qquad (2)$$

F_{Gly}^{in} and F_{Gly}^{out} are the molar flow of glycerol in the reactor inlet and outlet, respectively.

$$X_{gas}(\%) = 100 \times \frac{F_C^{in} - F_{C,liq}^{out}}{F_C^{in}} \qquad (3)$$

F_C^{in} is the carbon molar flow in the reactor inlet, and $F_{C,liq}^{out}$ is the carbon molar flow in the liquid products.

$$S_{H2}(\%) = 100 \times \frac{2 \cdot F_{H2}^{out}}{F_H^{gas}} \qquad (4)$$

F_{H2}^{out} and F_H^{gas} are the molar flow of hydrogen and hydrogen atoms in gas products, respectively.

$$Y_{H2}(\%) = 100 \times \frac{F_{H2}^{out}}{7 \cdot F_{Gly}^{in}} \qquad (5)$$

$$S_{alkanes}(\%) = 100 \times \frac{F_{C,alkanes}^{out}}{F_C^{gas}} \tag{6}$$

$F_{C,alkanes}^{out}$ and F_C^{gas} are the flow of carbon atoms in alkanes and in gas products, respectively.

$$Y_i(\%) = 100 \times \frac{F_{C,i}^{out}}{3 \cdot F_{Gly}^{in}} \tag{7}$$

where $F_{C,i}^{out}$ is the carbon molar flow in the liquid stream.

Additional experiments were carried out to evaluate the catalytic activity in the liquid phase WGS. The experiments were performed at 260 °C and 50 bar in the same reaction setup. The catalyst (0.2 g) was pretreated as for APR experiments. Deionized liquid water (0.04 mL/min) was fed together with pure CO (3.5 mL/min STP), which gave WHSV=12.0 h^{-1} (based on the liquid feed) and GHSV=1050 h^{-1} (based on CO). The gaseous products were swept from the reactor by flowing 40 mL/min helium. The resulting H_2O/CO mole ratio was 15, which corresponds to the theoretical value during APR process. Each run lasted 10 h, where stabilization was achieved after 5 h. The gas products were analyzed on-line by μGC. Conversion of CO and yields of CO_2 and CH_4 were calculated as follows:

$$X_{CO}(\%) = 100 \times \frac{F_{CO}^{in} - F_{CO}^{out}}{F_{CO}^{in}} \tag{8}$$

$$Y_{i,WGS}(\%) = 100 \times \frac{F_i^{out}}{F_{CO}^{in}} \tag{9}$$

F_{CO}^{in} and F_{CO}^{out} are the molar flows of CO in the reactor inlet and outlet, respectively, and F_i^{out} is the molar flow of product (CO_2 or CH_4) in the reactor outlet.

2.4. Mass transfer limitations

The existence of internal and external mass transfer limitations, was checked by the Weisz-Prater (equation 10) and the Mears (equation 11) criterion, respectively

$$\Phi_{WP} = \frac{(r_{obs}) \cdot \rho_{cat} \cdot r_P^2}{D_{G-W,eff} \cdot C_{G,s}} \tag{10}$$

$$\frac{MR}{n} = \frac{(r_{obs}) \cdot \rho_{bed} \cdot r_P}{K_C \cdot C_{G,s}} < 0.15 \tag{11}$$

where (r_{obs}) is the observed reaction rate (mol/s·kg$_{cat}$); ρ_{cat} is the catalyst density (kg/m^3); r_P is the catalyst particle radius (m); $D_{G\text{-}W,eff}$ is the effective diffusion coefficient of glycerol in water (m^2/s); and $C_{G,s}$ is the glycerol concentration at the catalyst surface (mol/m^3); ρ_{bed} is the packed bed density (kg/m^3); k_C is the mass transfer coefficient (m/s); and n is the reaction order. Mass transfer coefficient was estimated using the Chilton-Colburn analogy and Wilson-Geankoplis correlation for liquid mass transfer at very low Reynolds numbers [23].

Typical values that ensure the absence of internal mass diffusion limitations are as follows: $\Phi_{WP} < 6$ for a zero-order reaction; $\Phi_{WP} < 0.6$ for a first-order reaction; and $\Phi_{WP} < 0.3$ for a second-order reaction. In this work, Φ_{WP} and MR were calculated on the basis of the fastest reaction rate of $2.022 \cdot 10^{-4}$ mol/s·kg$_{cat}$ (measured at the beginning of the reaction) and largest particle size with an effective diffusion coefficient of $1.45 \cdot 10^{-9}$ m^2/s (estimated by Siddiqi-Lucas correlation, at 260 ℃/50 bar). Under the least favourable conditions, the obtained Φ_{WP} ($3.7 \cdot 10^{-3}$) and MR/n ($1.1 \cdot 10^{-4}$) confirm that the performed experiments were conducted in the absence of both internal and external mass transport limitations.

3. Results and Discussion

3.1. Catalyst basic characterization

The investigated catalysts showed mesoporous characteristics (Figure 2) with specific surface area (S_{BET}) values ranging from 125 to 146 m^2/g. After Pt loading into the CoAl spinel, surface area and pore volume size increased. S_{BET} increased up to 17%, being the highest at the lowest platinum content. After reduction, S_{BET} values decreased at the expense of larger pores. Also, it was observed that textural properties of the CoAl spinels were stabilised upon Pt loading. For instance, upon reduction, S_{BET} of catalyst CoAl and xPt/CoAl samples decreased by around 19% and 10%, respectively. Modification of the average pore size was also smaller in Pt loaded samples. Regarding the alumina supported reference catalyst (0.3Pt/Al), it showed the smallest pores. For this sample, both S_{BET} and pore size were preserved upon reduction.

Table 1. Physico-chemical properties of the catalysts.

Catalyst	Actual Pt [a] (wt.%)	S_{BET} (m^2/g) [b]	d_{pore} [b] (nm)	V_{pore} [b] (cm^3/g)	d_{spinel} [c] (nm)	d_{Co} [d] (nm)	(311) peak 2θ position [c] (°)	Lattice parameter (nm) [c]
CoAl	0	125 (102)	6.8 (11.8)	0.28 (0.38)	5.0	14.7	37.06	0.8042 ±0.0014
0.3Pt/CoAl	0.29	146 (131)	12.7 (14.8)	0.56 (0.52)	6.3	6.9	37.04	0.8052 ±0.0011
1Pt/CoAl	1.09	139 (126)	12.8 (14.9)	0.54 (0.51)	6.3	6.5	36.99	0.8063 ±0.0006
0.3Pt/Al	0.36	138 (138)	3.9 (4.0)	0.19 (0.20)	n.d.	n.d.	n.d.	n.d.

[a] from ICP-AES.

[b] from nitrogen isotherms. In parenthesis, values for the reduced samples.

[c] from XRD of the calcined samples.

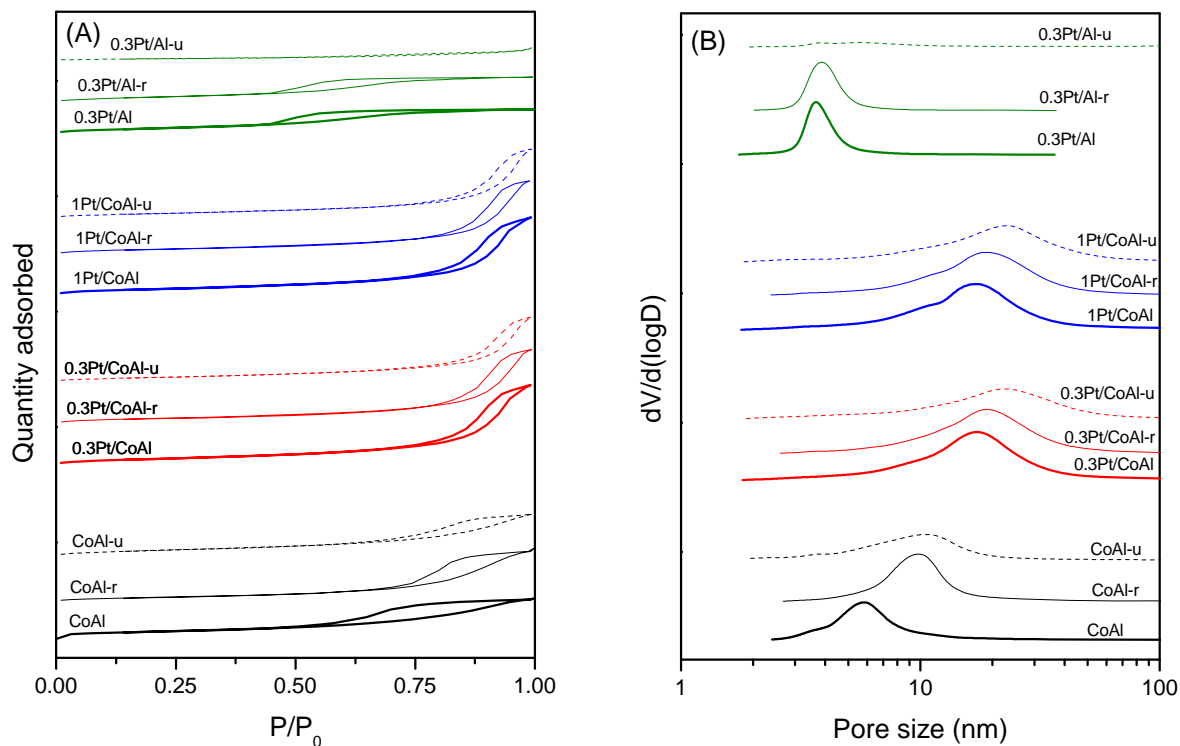[d] metallic cobalt size from XRD of the reduced samples.

Figure 2. Nitrogen isotherms (A) and pore size distribution (B) of the calcined, reduced (-r) and spent (-u) samples.

XRD patterns are shown in Figure 3. Independent of the support, none of the Pt-containing samples showed any diffraction peak of platinum species, what pointed to a high Pt dispersion, as expected by the low loadings applied ($1000 \times$ Pt/Co mole ratio=2.3-7.7). XRD pattern of catalyst CoAl matched with the reference cobalt aluminate (PDF 00-044-0160) and cobalt oxide (PDF 00-042-1467) spinel. xPt/CoAl samples showed similar diffraction spectrum to bare CoAl. However, after Pt loading, the main diffraction peak slightly shifted to lower angles with a concomitant increase of the unit cell (Table 1). The spinel crystallite size also increased from 5 nm to 6.3 nm. On the contrary, size of metallic cobalt crystallite decreased by half. Catalyst 0.3Pt/Al showed characteristics peaks of γ-alumina with a clear baseline elevation indicative of its amorphous nature. Moreover, in accordance with previous characterisation data, its diffraction pattern was mimetic to the calcined counterpart. Regarding the reduced xPt/CoAl samples, diffraction peaks of spinel phase remained (probably as $CoAl_2O_4$) [7], and diffraction peaks of metallic Co arose, whereas any signal of Pt species was absent.
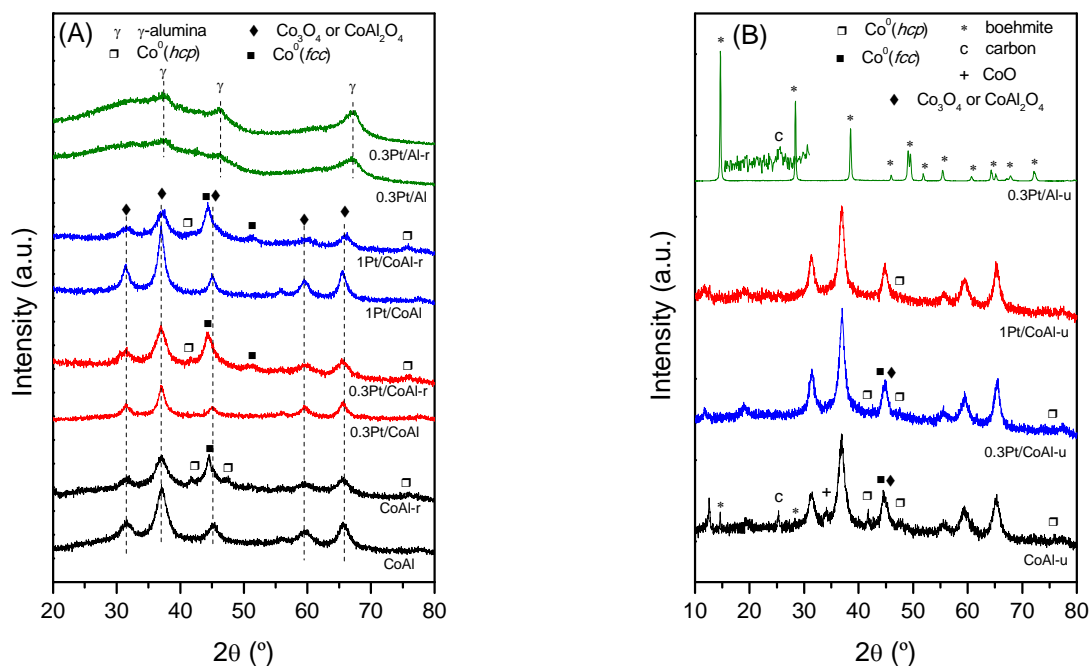
Figure 3. (A) XRD patterns of the calcined and reduced (-r) samples; (B) spent (-u) samples.

The local structure of the aluminium cations in the calcined catalysts was studied with solid-state ^{27}Al NMR. The obtained spectra are displayed in Figure 4 and quantification results of Al^{3+} ions in different coordination structures are shown in the inset table. Bare alumina presents three peaks at 7.5, 33.6 and 61.8 ppm, related to octahedral (Al_O), pentahedral (Al_P) and tetrahedral (Al_T) Al^{3+} species, respectively [24]. CoAl spinel, however, showed only two peaks at 6.9 and 71.8 ppm, strongly prevailing the octahedral symmetry (Al_O/Al_T=96/4). Also, the low symmetry of the main peak of CoAl indicated different Al^{3+} surrounding environments. The ^{27}Al NMR spectra of xPt/CoAl samples revealed the existence of three Al^{3+} species (at 5.9, 33 and 61.7 ppm, respectively). Although at a very low relative intensity (about 8% for both samples), the peak at around 33 ppm representing Al^{3+} ions in unsaturated pentahedral coordination (Al_P) has emerged in the bimetallic samples, which was not detected in bare CoAl. Data compiled in Figure 3 reflect that both bimetallic assays contained relatively less amount of Al_O as compared to bare CoAl, suggesting that Pt ensembles anchor on these sites. Also, in comparison to bare CoAl, Al_T and Al_O peaks of xPt/CoAl samples shifted to the right. The higher the Pt loading, the higher the shift. These results clearly indicate that the deposition of platinum ions caused changes in the distribution and coordination of Al_O sites of the cobalt aluminate spinel.
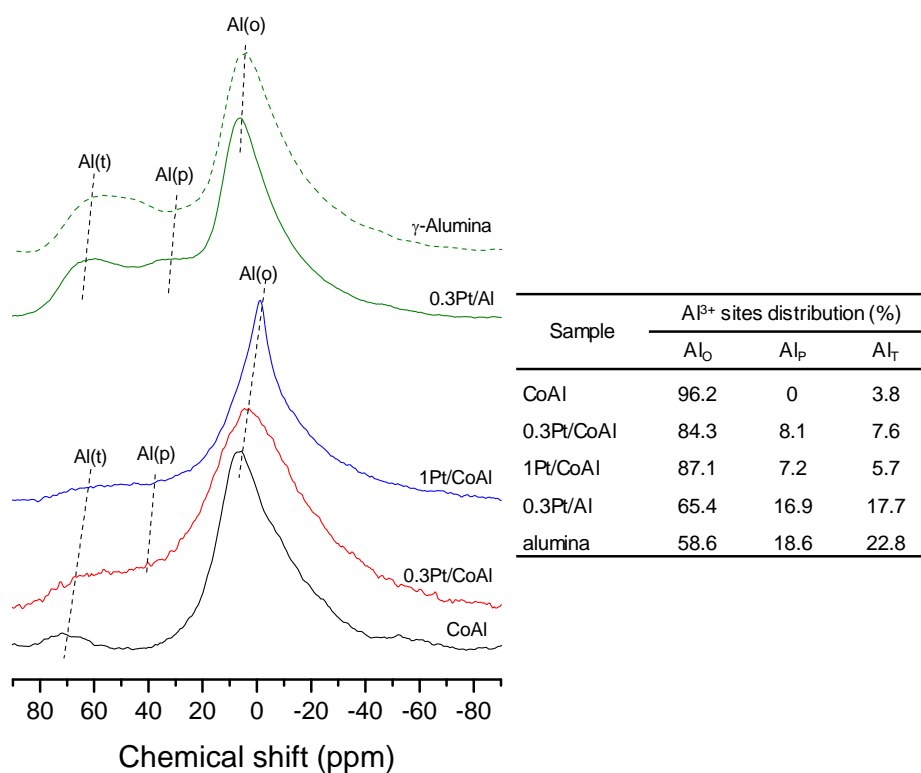
13

Sample	Al³⁺ sites distribution (%)		
	Al_O	Al_P	Al_T
CoAl	96.2	0	3.8
0.3Pt/CoAl	84.3	8.1	7.6
1Pt/CoAl	87.1	7.2	5.7
0.3Pt/Al	65.4	16.9	17.7
alumina	58.6	18.6	22.8

Figure 4. ^{27}Al-NMR spectrum of calcined samples, and the distribution of differently coordinated Al^{3+} sites (from the peak areas).

The reducibility of the catalysts was studied by H_2-TPR (Figure 5). The reduction profile of 0.3Pt/Al showed three very low intensity peaks. The peak at 227 ºC was ascribed to the reduction of highly dispersed platinum species with little interaction with the support, while the peak at 375 ºC was ascribed to the reduction of platinum species highly interacting with alumina [25]. The high temperature peak, at around 660 ºC, was related to reduction of alumina, assisted by hydrogen spillover on Pt [26]. The reduction profile of CoAl sample showed four peaks. The low temperature peaks, centred at 292 and 413 °C, were ascribed to the reduction of Co^{3+} to Co^{2+}. Peak at 292 ºC was related to the surface cations without any interaction with the support, while peak at 413 ºC was ascribed to the reduction of Co^{3+} species in close interaction with the support. The huge peak centred at 594 ºC, was assigned to Co^{2+} reduction to Co^0, and peak at 783 ºC to the reduction of cobalt ions in the cobalt aluminate ($CoAl_2O_4$) phase [7]. After Pt loading, a low temperature peak emerged, at 192 and 157 ºC, for 0.3Pt/CoAl and 1Pt/CoAl, respectively. Quantification of these peaks is given in Table 2. For both bimetallic samples, the hydrogen consumption of these peaks exceeded the theoretical H_2 consumption of PtO_X species (PtO species were assumed), what suggested the concomitant Co^{3+} to Co^{2+} reduction of free surface cations promoted by platinum, due to hydrogen spillover from the Pt^0 surface. As observed, the promotional effect was largest at the lowest Pt loading (0.3 wt.%). For instance, at the lowest Pt loading, the reduction temperature of Co^{2+} to Co^0 decreased

by around 31 ºC, and that of cobalt ions in the spinel phase was reduced by around 47 ºC. It should be noted, however, that addition of Pt at 1 wt.% produced the opposite effect in the less reducible Co species, as revealed by the increased reduction temperature of the Co^{2+} to Co (637 vs. 563 ºC) and that of Co ions in the spinel phase (820 vs. 736 ºC). The cobalt reducibility at 600 ºC varied from 62.6% for monometallic CoAl to 68.6% for 0.3Pt/CoAl (Table 2), indicating the promotional effect of Pt. In conclusion, in the 0.3Pt/CoAl system reducibility of the metal species (Pt, Co) was significantly promoted, as deduced from the increased low temperature hydrogen consumption, likely due to a strong Pt-Co interaction. This is in line with the increased amount of available metallic Co with respect to reference CoAl (Table 2). The smaller size of Co^0 of the bimetallic samples, as estimated by XRD, could be also involved. Also, available metallic Pt sites increased proportionally to Pt loading. Thus, we hypothesize that Pt-Co interaction, especially at low Pt loadings, not only promoted the reducibility of the catalyst but also increased the amount of available metallic Co species.

Table 2. H_2-TPR, H_2 chemisorption and surface acidity data.

Catalyst	Total H_2 uptake $(mmol_{H2}/g)$	Low temperature peak H_2 uptake $(mmol_{H2}/g)$	Degree of reduction [a] (%)	Exposed Pt^{0} [b] $(at._{Pt}/g_{cat})$	Exposed Co^{0} [b] $(at._{Co}/g_{cat})$	Surface acid sites density [c] $(\mu mol_{NH3}/m^2)$
CoAl	7.04	n.a.	62.6	0	$23.0 \cdot 10^{18}$	0.51
0.3Pt/CoAl	7.29	0.516 (0.0149)	68.6	$5.2 \cdot 10^{18}$	$30.4 \cdot 10^{18}$	0.56
1Pt/CoAl	7.36	0.659 (0.0559)	65.3	$20.7 \cdot 10^{18}$	$25.5 \cdot 10^{18}$	0.68
0.3Pt/Al	0.35	0.0195 (0.0185)	n.d.	$6.9 \cdot 10^{18}$	0	0.34

In parenthesis the theoretic amount assuming PtO species.

[a] H_2 consumption at 600ºC with respect to 950 ºC (theoretical consumption ascribed to PtO substracted); [b] from H_2 pulse chemisorption; [c] from ammonia mass gain.
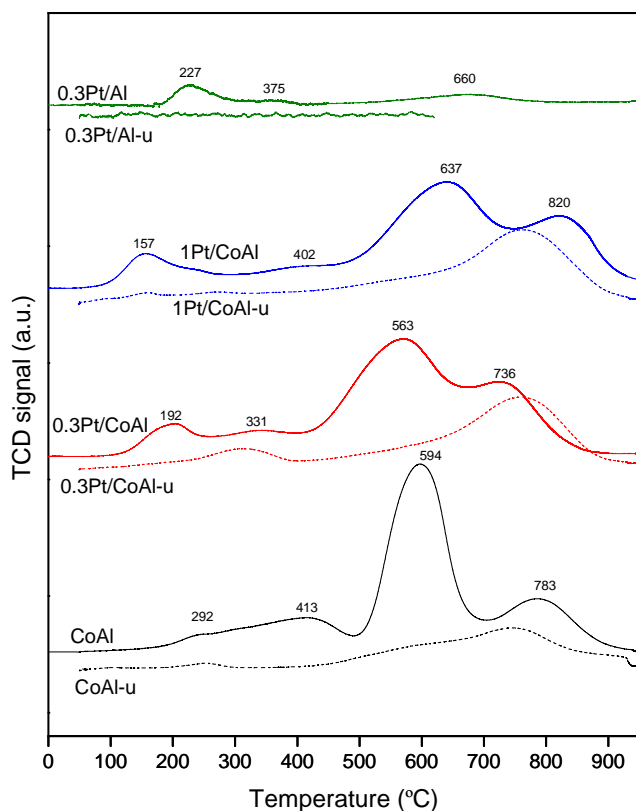
Figure 5. H$_2$-TPR profiles for the fresh and spent (-u) samples.

Regarding the density of acid sites of the reduced samples (Table 2), monometallic Pt sample showed the lowest values (0.34 $\mu mol_{NH3}/m^2$) which was about 1.5-2 fold lower than that of Co-containing samples. It was observed that among Co-containing samples, addition of Pt linearly increased the acid sites density.

XPS measurements were carried out to investigate the surface composition and chemical valence state of the active species. The binding energies (BE) of the Al, Co and Pt species and the surface Co/Al atomic ratios are reported in Table 3. The Co 2p X-ray photoelectron spectra for the CoAl and xPt/CoAl reduced samples are shown in Figure 6 (Al 2p and Pt 4d$_{5/2}$ spectra are given in Figure S1, Supplementary Information). The characteristic Co 2p doublet (Co 2p$_{3/2}$ and Co 2p$_{1/2}$) due to spin-orbit splitting was observed in all samples. The spectra were deconvoluted into Co^0, Co^{2+} and shake up satellites but no peaks were assigned to Co^{3+}. The most interesting features were obtained from the reduced assays. Al 2p level binding energy was measured at 74.2 eV, which is typically ascribed to Al$_2$O$_3$ species. Co 2p peaks, in the xPt/CoAl system, shifted to higher binding energies in comparison with CoAl catalyst. This reflected a charge transfer to adjacent electronegative Pt atoms from slightly less electronegative Co, lowering electron density at the Co site [27]. Thus, supported the above noted Pt-Co interaction in the investigated system. It is known that the Al 2p photoelectron line of alumina can mask the most prominent photo-emitted electron of platinum (Pt 4f) [28].

Table 3. Results from XPS analysis.

Catalyst	Al 2p (eV)	Co 2p$_{3/2}$ (eV)		Pt 4d$_{5/2}$ (eV)		Surface Co/Al [a]	Bulk Co/Al [b]
		Co^{2+}	Co^0	Pt^{2+}	Pt^0		
CoAl	75.6 (74.2)	781.6 (781.3)	n.d. (778.0)	n.a.	n.a.	0.266 (0.139)	0.634
0.3Pt/CoAl	74.2 (74.2)	781.1 (781.6)	n.d. (778.2)	316.8 (n.d.)	n.d. (314.0)	0.271 (0.184)	0.633
1Pt/CoAl	74.2 (74.2)	781.2 (781.5)	n.d. (778.2)	317.7 (n.d.)	n.d. (314.2)	0.271 (0.186)	0.623
0.3Pt/Al	74.0 (73.5)	n.d.	n.d.	315.5 (n.d.)	n.d. (313.8)	n.d.	n.d.

Values in parenthesis for reduced samples.

[a] from XPS of calcined samples; [b] from ICP-AES.

However, in spite of the low platinum content, binding energies of the $4d_{5/2}$ level could be recorded at 314.0 ±0.2 eV for the bimetallic catalyst, what confirmed the existence of Pt^0 phase.

According to Table 3, the surface was enriched in Al ions (decrease in Co/Al evaluated by XPS) as compared to bulk composition (evaluated by ICP-AES), what could be attributed to the lower surface free energy of Al as compared to Co [29]. Moreover, Co/Al atomic ratio on surface decreased upon reduction. This behaviour has been related to the incorporation of metallic species into the porous structure [30], which would also explain the decrease in pore volume. Also, it is interesting to note the higher Co/Al values measured for the bimetallic assays (as compared to parent CoAl) and, regardless of their calcined or reduced state.
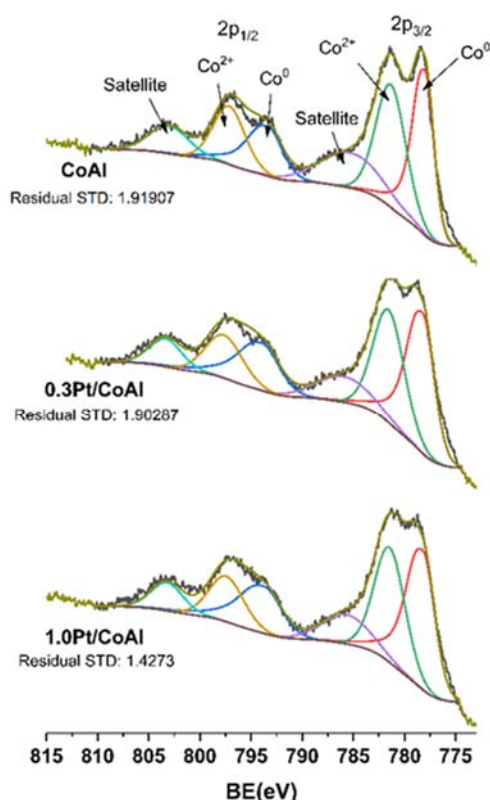

Figure 6. Deconvoluted XPS spectra for Co 2p in reduced samples.

3.2. APR of glycerol

The activity of the prepared catalysts in the Aqueous-Phase Reforming was investigated using 10 wt.% glycerol/water feedstream. Two preliminary experiments (not shown) were carried out, first, with no catalyst loaded into the reactor and second, with the reactor loaded with bare γ-alumina (prepared by calcination in air at 500 ºC for 4 h of aluminium(III) nitrate nonahydrate). Both runs showed almost null activity, what reflected the critical role of the metallic function during the glycerol conversion by APR (at the experimental conditions carried out in this work). Figure 7 shows the evolution of glycerol total conversion (X_{Gly}) and carbon conversion to gas (X_{gas}) with TOS by the

investigated catalysts. The investigated catalysts proved high glycerol APR activity with a very high conversion of glycerol (above 99%) during the whole test. Also, Pt-doped samples remained stable throughout the entire test (100 h TOS) whereas CoAl suffered a weak deactivation at above 70 h TOS. Indeed, the reported APR activity of the CoAl spinel supported catalysts can be deemed very favourable as compared to data reported in literature [17,20].
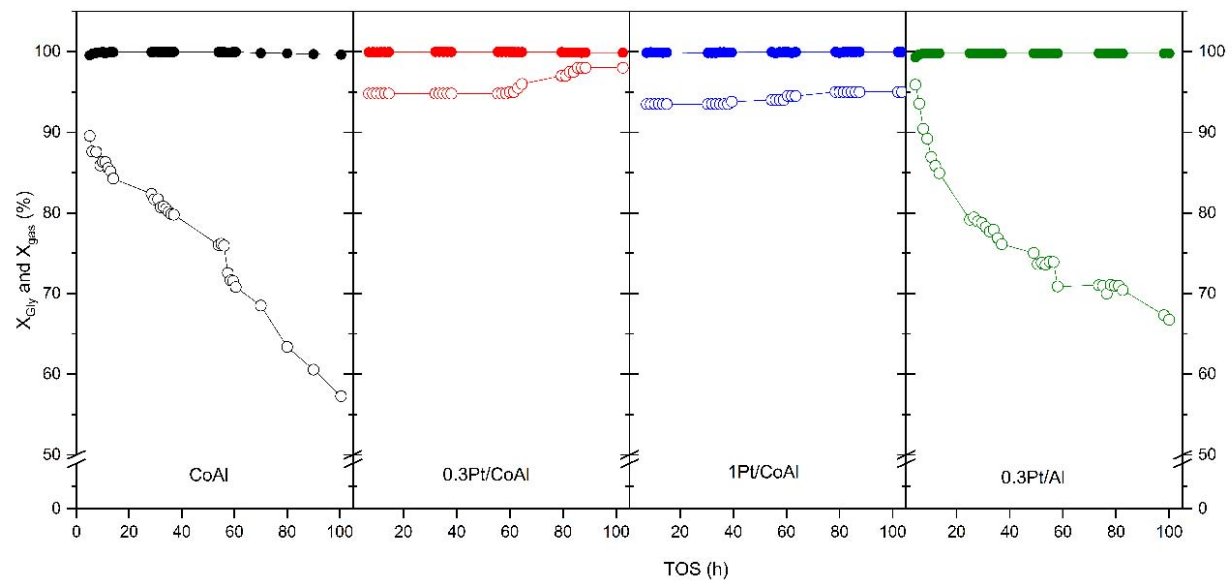
Figure 7. X_{Gly} (solid circles) and X_{gas} (open circles) evolution with TOS. Reaction conditions: 260 ºC/50 bar, 10 wt.% glycerol, WHSV=0.68 h-1

Significant differences existed in the carbon conversion capability of the investigated catalysts. Again, both Pt-Co bimetallic catalysts showed the highest and more stable carbon conversion to gas (around 95%). Catalyst CoAl, with an inital X_{gas} value of 89.5% suffered 36% decay (X_{gas} of 57.3% at 100 h TOS). Reference 0.3Pt/Al catalyst also displayed moderate decay in X_{gas}, from 95.9% at the beginning of the reaction to 66.8% at 100 h TOS (30% decay). As previously noted, bimetallic catalysts showed very stable operation over 100 h TOS, moreover, a subtle increase in X_{gas} was appreciated. Overall, such stable performance in the glycerol conversion and gasification suggested a relevant role of Pt species in catalyst stabilisation.

Table 4. Gaseous and liquid products characteristics at 10 h/100 h TOS. Reaction conditions: 260 ºC/50 bar, 10 wt.% glycerol, WHSV=0.68 h^{-1}.

Catalyst	Gas products					Liquid products				
	S_{H2} (%)	$S_{alkanes}$ (%)	Y_{H2} (%)	$[H_2]$ (%)	H_2/CO_2	$Y_{ethanol}$ (%)	$Y_{acetone}$ (%)	$Y_{propanols}$ (%)	$Y_{propionic\ acid}$ (%)	$F_{C,liq}$ ($\mu mol_C/min$)
CoAl	67/86	29/16	55/89	61/78	2.8/4.7	0.2/0	2.8/2.6	2.5/1.9	5.5/13.8	9.0/28.4
0.3Pt/CoAl	49/53	34/38	37/44	50/52	2.0/2.0	0/0	1.1/0.9	0.5/0.4	0/0	3.5/1.3
1Pt/CoAl	32/49	40/36	21/36	37/49	1.8/1.8	0/0	0.6/0.4	3.4/2.7	0/0	4.3/3.3
0.3Pt/Al	65/65	31/29	57/46	60/62	2.7/2.8	1.4/4.1	0.9/1.0	0.7/1.7	0/0	8.8/22.1

The carbon balance was above 97% for all the experiments.

For the sake of simplicity, the details of gaseous products and liquid products are given at 10 h and 100 h TOS, and can be found in Table 4 (the evolution with TOS for the complete run is shown in Figure S2, Supporting Information). Hydrogen was the main gaseous product for all the tested catalysts, with concentrations of around 60% by CoAl and 0.3Pt/Al, which dropped off to around 38% after incorporation of 1 wt.% Pt. Selectivity to hydrogen was also highest for these assays. CO_2 was the second most abundant gas product, throughout the whole reaction time. Light alkanes (mainly methane) were formed in appreciable amounts, especially by the bimetallic catalysts. We believe such product distribution might be due to factors such as: (i) the very low spatial velocity which enabled a large contact time between catalyst and reactants, pushing forward the hydrogenation reactions of the liquid intermediates, and (ii) the high reaction temperature employed in this work, where the CO hydrogenation is thermodynamically and kinetically favoured [31]. According to reaction 3, the theoretical H_2/CO_2 ratio for the glycerol APR is 7/3. Lower values indicated hydrogen was consumed in parallel reactions (i.e. hydrogenation), while higher values indicated glycerol was partially reformed, to yield intermediates that release hydrogen but hold carbon atoms in the skeleton. It was observed that both monometallic samples gave the highest H_2/CO_2 values (> 2.4), while this ratio decreased to 2.0 and 1.3, for 0.3Pt/CoAl and 1Pt/CoAl, respectively. This behaviour coincided with their higher alkane production. It is likely that the small crystallites of cobalt particles and Pt-Co alloying in the bimetallic samples was involved in such methane production [32]. This behaviour was much more marked at the longest TOS ($S_{alkanes}$ 36-38% vs. 16%).

The yield to liquid product, evaluated as carbon moles in the liquid compounds ($F_{C,liq}$), was significantly low under the investigated conditions (Table 4). These results agree with the high conversion to gas achieved by these catalysts (Figure 7). It is worth pointing out the significantly higher liquid flow rate obtained by monometallic catalysts (CoAl and 0.3Pt/Al) as compared to bimetallic samples, reflecting the decisive role of catalyst formulation on product distribution. Moreover, $F_{C,liq}$ varied with TOS, especially for monometallic assays, which showed three-fold increase during the catalytic run, showing a clear trade-off with X_{gas} (Figure 7). Interestingly, $F_{C,liq}$ for bimetallic samples remained almost constant, as an evidence of its stability in the glycerol APR.

Liquid intermediates obtained by the cobalt-containing catalysts comprised mainly C3 (i.e. acetone, propanols) compounds, what reflected a low decarbonylation activity. With respect to reaction pathways, it seemed that Path II was predominant (Figure 1), which proceeded though glycerol dehydration reaction over acid sites. The highest amount of C3 liquid intermediates was attained by catalyst CoAl with the concomitant increase of the H_2/CO_2 ratio, at above theoretical values. CoAl was the unique assay that contained propionic acid in the liquid stream, which is formed through the dehydrogenation of 1-propanol and subsequent Cannizzaro reaction [33]. Regarding the reference

catalyst 0.3Pt/Al, it produced comparable yields of C2 and C3 products. The main liquid product of the monometallic 0.3Pt/Al catalyst was ethanol, a secondary product obtained via the decarbonylation of hydroxyacetone, and favoured by metallic function. Regarding the xPt/CoAl assays, at the lowest Pt/Co ratio, yield to acetone dominated. As Pt loading increased, 2-propanol became the main liquid compound, which was likely formed through the hydrogenation of acetone.

At high values of TOS the intensification of the dehydration route for both monometallic catalysts was evidenced by an increased yield of liquid products ($F_{C,liq}$) with significantly higher selectivity to propionic acid (CoAl) and ethanol (0.3Pt/Al). Gas phase product distribution also changed with TOS, especially for the monometallic CoAl catalyst. This case, the selectivity to H_2 notably increased, up to 86%. It is noteworthy that although X_{gas} declined with TOS for catalyst CoAl, the H_2 yield increased (up to 89% for CoAl). However, for the monometallic catalyst 0.3Pt/Al selectivity to H_2 remained unchanged and thus, the H_2 yield decreased with TOS. Interestingly, bimetallic xPt/CoAl system showed a more stable performance with TOS. For instance, yield to liquid products remained at similar values, or even diminished. Concomitantly, the yield to H_2 increased to around 50%.

The obtained product distribution in APR experiments was hardly correlated with the surface acidity, conceivably due to the small differences among them. Instead, it was suggested that the product distribution depended on the balance between acid sites and metallic sites.

3.3. Liquid phase WGS

It is widely recognized that WGS reaction is a key step in the APR of polyols [9,34]. In order to gain knowledge on the effect of Pt addition in the WGS activity of CoAl catalysts, additional experiments were performed under the same conditions utilised in APR reaction, and at a water/CO mole ratio of 15/1 in the feedstream. Figure 8 displays data obtained at 10 h TOS (stability was achieved after 5 h TOS). Interestingly, bare CoAl catalyst outperformed the WGS benchmark Pt catalyst [35,36], with a CO conversion of around 51.2 and 29.9%, respectively. From Figure 8 it can be seen that WGS activity of the bimetallic catalysts progressively increased with Pt loading, in line with previous reports [11]. The promotional effect in WGS of Co-Pt alloys has been explained in terms of their water dissociation ability and lowering of CO binding energy [37]. Also, data in Figure 8 reflected that H_2 and CO_2 were the main products over all the assayed catalysts. Methanation activities were very low, as follows: 0.3Pt/Al (0.3%) < 0.3Pt/CoAl (0.9%) < CoAl (1.5%) < 1Pt/CoAl (1.9%). Indeed, under the investigated conditions, (i.e. feeding contained only CO/water), hydrogenation of CO to methane was negligible, as due to the low availability of the in-situ produced hydrogen. Further investigation should consider reaction conditions more representative of real APR operation to elucidate whether high hydrogen availability could overcome such CO hydrogenation limitations.
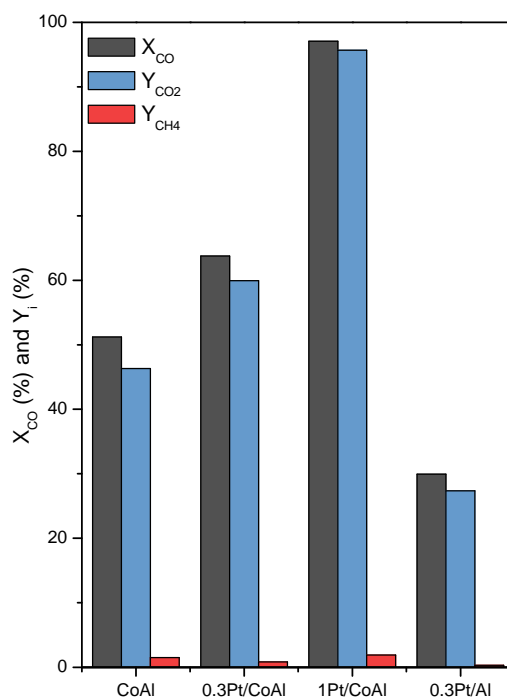
Figure 8. CO conversion and products yield in liquid phase WGS reaction at TOS= 10 h.
Feedstream: $H_2O/CO=15/1$ mole ratio.

3.4. Characterization of spent catalysts

Catalysts used in the APR of glycerol (100 h TOS) were thoroughly characterised in order to study their stability. XRD diffractograms are displayed in Figure 3B. As occurred in the parent fresh samples, no peaks of platinum were observed for any of the spent catalysts. Cobalt-containing catalysts showed wide and asymmetric peaks, as in the fresh samples. From data summarised in Table 5 an increase of the spinel crystal size was observed, with a maximum increase of 38% measured for catalyst CoAl. Characteristic peaks of metallic cobalt could be still detected, though, too weakly to perfom quantitative analysis. Also, boehmite phase was identified in both monometallic catalysts, specially in sample 0.3Pt/Al. Indeed, the spinel structure can hinder the hydration of alumina to bohemite. Taking into consideration that diffraction peaks of boehmite were not observed for the bimetallic samples, it is likely that the presence of Pt could further inhibit the hydration. Also, it is worth noting that only monometallic assays, and particularly catalyst CoAl, exhibited the characteristic diffraction peak of carbon, at $2\theta = 25.5°$.

Table 5. Some characteristics of the spent catalysts.

Catalyst	S_{BET} (m²/g)	V_{Pore} (cm³/g)	d_{pore} (nm)	d_{spinel} (nm) [a]	Leached metals (wt.%)			Surface total metal (at.$_{(Pt+Co)}$/g$_{cat}$)	Total H₂ uptake (mmol$_{H2}$/g)	% oxidized (Co species) [b]	Carbon deposits (μmol$_C$/g$_{cat}$) [c]
					Al	Co	Pt				
CoAl	142 (102)	0.309 (0.375)	7.6 (11.8)	6.9 (5.0)	0.6	2.7	n.a	$1.1 \cdot 10^{18}$ ($23 \cdot 10^{18}$)	3.07	35.7	13.5
0.3Pt/CoAl	113 (131)	0.457 (0.521)	13.5 (14.8)	7.8 (6.3)	0.3	1.6	0.1	$6.4 \cdot 10^{18}$ ($35.6 \cdot 10^{18}$)	4.37	27.1	1.9
1Pt/CoAl	113 (126)	0.485 (0.514)	14.5 (14.9)	7.2 (6.3)	0.1	5.7	0.06	$40 \cdot 10^{18}$ ($46.2 \cdot 10^{18}$)	5.02	29.6	1.2
0.3Pt/Al	43 (138)	0.093 (0.198)	7.7 (4.0)	n.d.	0.4	n.a	0.02	$6.5 \cdot 10^{18}$ ($6.9 \cdot 10^{18}$)	0	n.a.	2.7

Values in parentheses for reduced non-used samples. [a] from XRD. [b] from TPR up to 600 ºC. [c] from TPH.

The textural properties of spent catalysts are shown in Figure 3, and summarised in Table 5. Catalyst 0.3Pt/Al suffered the most drastic alterations with around 70% decrease in the specific surface area and pore volume. This behaviour was certainly ascribed to formation of boehmite [38]. CoAl spinel showed the opposite behaviour with a substantial increment of its $S_{BET,}$ likely aided by an important reduction of the average pore size (from 11.8 to 7.6 nm) and minor decrease of its pore volume. Finally, the bimetallic xPt/CoAl catalysts showed an intermediate behaviour. That is, both specific surface area and pore volume decreased after usage, though moderately (within 6-14% decrease). Pore size hardly varied, indicative of a higher textural and surface stability of bimetallic catalysts compared to monometallic ones.

One of the most promising results of the investigated assays is their limited metal (Al, Co and Pt) leaching (Table 5) even though the long run duration (100 h). The amount of Pt and Al leached out from the fresh catalyst was less than 0.1% and 0.6%, respectively. Co leaching is an issue during the aqueous phase reforming [37]. Our CoAl spinels leached restrained Co leaching with values in the 1.6 − 5.7% of the cobalt loaded. For instance, our results are more advantageous than those previously reported in the literature with Co leaching of around 8.9% from carbon nanofiber supported catalysts and during 24 h of ethylene glycol APR [39]. Thus, it is clear that the effectiveness of alternative catalysts formulations requires a careful assessment in order to better anchor the metal.

From the H_2-TPR profiles of the spent catalysts (Figure 5) some hydrogen consumption at below 600 ºC was evidenced, what reflected that oxidation of the metal species (i.e. fresh catalysts were reduced at 600 ºC) occurred. As expected, 0.3Pt/Al was not oxidized. It is known that oxidation of Pt in aqueous phase is difficult, even in the presence of hydrogen [40]. This was also supported by the fact that the amount of available metal after APR was preserved for catalyst 0.3Pt/Al (Table 5). Taking this into consideration, we have assumed that Pt-Co alloys were also resistant to oxidation under APR conditions [37], thus, we hypothesize that the reduction peaks at below 600 ºC were due to oxidized cobalt species not interacting with Pt. The contribution of coke hydrogenation should not be discarded, as suggested by the identification of carbonaceous deposits by Raman. Thus, the oxidation percentages of Co given in Table 5 could be somewhat overestimated. Also, the reduction peak at about 750 ºC observed for all the cobalt containing samples, was ascribed to the reduction of cobalt species in the $CoAl_2O_4$ spinel phase, not reduced by the reduction before the catalytic run. Interestingly, bimetallic catalysts suffered less oxidation under APR conditions than the parent monometallic CoAl. In quantitative terms, for the most favorable assay, the oxidation of cobalt species was reduced by around 25% upon Pt doping (from 35.7 to 27.1%, for CoAl and 0.3Pt/CoAl, respectively). This behavior was also consistent with the dramatic decrease in the exposed metal atoms (95% decrease) of the former.
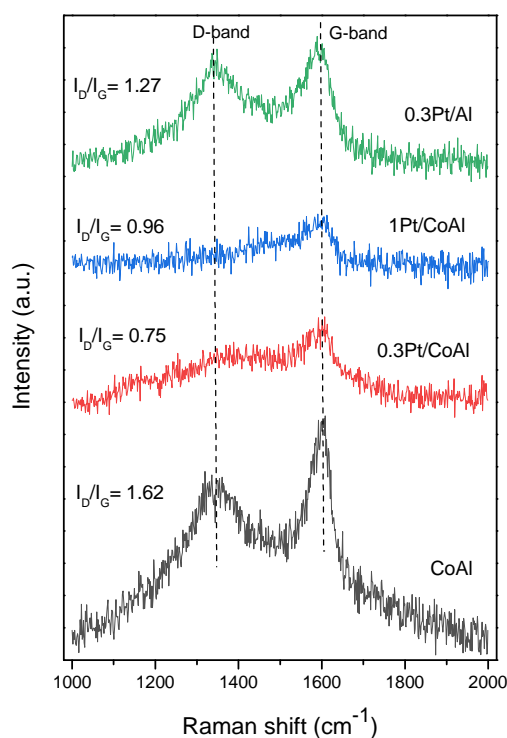
Figure 9. Raman spectra of the spent catalysts.

The nature of the above mentioned carbon deposits was investigated by Raman spectroscopy. The Raman spectra (Figure 9) of both monometallic catalysts showed two bands (namely G and D). G band (in the range 1594-1598 cm^{-1}) corresponded to ordered graphite-like structures while D band (about 1342 cm^{-1}) was associated to the disordered carbon, generally amorphous carbon [41]. The spectra of the spent bimetallic catalysts were quite diferent and showed very low intensity of both bands, indicating negligible formation of carbonaceous deposits on the catalyst surface. It seemed clear that the strong Pt-Co interaction inhibited the coke formation during APR of glycerol [42]. According to the ratio of intensity of D-Band to G-Band (I_D/I_G), it could be concluded that the carbonaceous deposits on all the spent catalysts were predominantly amorphous, as I_D/I_G values were above or near unity. In the case of CoAl catalysts, the amorphous carbon would coexist with graphitic carbon, as suggested the diffraction peak at $2\theta = 25.5°$. The absence of diffraction peaks of graphitic carbon for bimetallic catalysts must be related to the low amount of deposits.
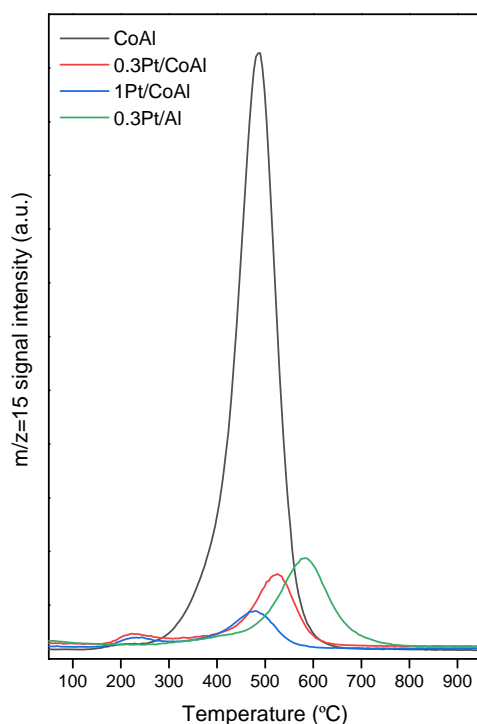
Figure 10. TPH profiles of the spent catalysts.

The carbonaceous deposits were quantified by TPH coupled to MS. Figure 10 shows the evolved methane (m/z=15 signal) with temperature. Methane was formed from the hydrogenation of the surface carbonaceous materials. The amount of surface carbon deposits ($\mu mol_C/g_{cat}$) are given in Table 5. Methane was released in the 200-700 ºC range. Such a wide temperature range suggested the presence of different reactivity carbonaceous species, in agreement with the presence of two Raman peaks. Low temperature peak (at around 200 ºC) can be ascribed to hydrogenation of the more amorphous carbon, while the high temperature peak (between 500 and 600 ºC) was attributed to the hydrogenation of more polymerized carbonaceous deposits that need higher temperatures for its removal [43]. It is interesting to note that only Pt-containing assays showed the low temperature peak, what suggests it could correspond to the hydrogenation of carbon deposited in the proximity of well dispersed Pt centers, which could dissociate and spillover hydrogen on the surface and favour hydrogenation of the carbonaceous precursor. Therefore, the high temperature peak was ascribed to the hydrogenation of carbon deposits located in farthest positions from the metallic centers [44]. Notably, catalysts CoAl showed the largest methane yield, of around 13.5 $\mu mol_C/g_{cat}$. It was very significant the attained reduction upon Pt loading, with around ten-fold decrease (1.2-1.9 $\mu mol_C/g_{cat}$), in line with previous XRD and Raman results.

4. Conclusions

We have investigated bare and Pt-impregnated cobalt aluminate catalysts for the activity and stability in glycerol valorisation by Aqueous-Phase Reforming. The characterization of these samples revealed

that Pt loading stabilized the textural and structural properties of the CoAl spinel-supported catalysts. In addition, at the lowest loading (i.e. 0.3%) Pt-Co interactions promoted the reduction and dispersion of cobalt species. The investigated catalysts presented very high conversion of glycerol and conversion to gas during the first 10 h TOS. This catalytic behaviour was sustained up to 100 h TOS by the bimetallic catalysts. The incorporation of Pt to CoAl also increased methane production. Even so, hydrogen was the main product for all the assayed catalysts, followed by CO_2. The synergistic effect between Pt and Co was also confirmed in the liquid phase WGS activity as bimetallic catalysts showed higher activity than monometallic ones.

Examination of spent catalysts revealed that xPt/CoAl bimetallic catalysts preserved their structural and textural properties, whereas APR conditions significantly deteriorated those of monometallic ones. The total available metal atoms decreased considerably for catalysts without or with a lower platinum content. H_2-TPR confirmed the oxidation of metallic cobalt active centres, which was probably the first step in leaching this metal. Amorphous carbonaceous deposits were detected by Raman spectroscopy and quantified via methane formation using temperature-programmed hydrogenation. Obtained results corroborated that Pt-containing catalysts formed less amount of carbon deposits, as they could be hydrogenated by hydrogen spillover from Pt.

Largely, catalytic features of Pt-Co samples evidenced that bimetallic catalysts are suitable for glycerol APR. However, and based on the presented results, further study should be carried out to prevent cobalt oxidation and leaching.

References

[1] M. Pagliaro, R. Ciriminna, H. Kimura, M. Rossi, C. Della Pina, From Glycerol to Value-Added Products, Angew. Chem. Int. Ed. 46 (2007) 4434-4440

[2] U.I. Nda-Umar, I. Ramli, Y.H. Taufiq-Yap, E.N. Muhamad, An Overview of Recent Research in the Conversion of Glycerol into Biofuels, Fuel Additives and other Bio-Based Chemicals, Catalysts 9(1) (2019) 15

[3] R.D. Cortright, R.R. Davda, J.A. Dumesic, Hydrogen from catalytic reforming of biomass-derived hydrocarbons in liquid water, Nature 418(6901) (2002) 964-7

[4] I. Coronado, M. Pitínová, R. Karinen, M. Reinikainen, R.L. Puurunen, J. Lehtonen, Aqueous-phase reforming of Fischer-Tropsch alcohols over nickel-based catalysts to produce hydrogen: Product distribution and reaction pathways, Appl. Catal. A:Gen. 567 (2018) 112-121

[5] J. Remón, L. García, J. Arauzo, Cheese whey management by catalytic steam reforming and aqueous phase reforming, Fuel Process. Technol. 154 (2016) 66-81

[6] A.S. Oliveira, J.A. Baeza, L. Calvo, N. Alonso-Morales, F. Heras, J. Lemus, J.J. Rodriguez, M.A. Gilarranz, Exploration of the treatment of fish-canning industry effluents by aqueous-phase reforming using Pt/C catalysts, Environ. Sci.: Water Res. Technol. 4 (2018) 1979-1987

[7] A.J. Reynoso, J.L. Ayastuy, U. Iriarte-Velasco, M.A. Gutiérrez-Ortiz, Cobalt aluminate spinel-derived catalysts for glycerol aqueous phase reforming, Appl. Catal. B:Environ. 239 (2018) 86-101

[8] S. Jeon, Y.M. Park, J. Park, K. Saravanan, H.K. Jeong, J.W. Bae, Synergistic effects of Nb_2O_5 promoter on Ru/Al_2O_3 for an aqueous-phase hydrodeoxygenation of glycerol to hydrocarbons, Appl. Catal. A:Gen. 551 (2018) 49-62

[9] R. He, R.R. Davda, J.A. Dumesic, In Situ ATR-IR Spectroscopic and Reaction Kinetics Studies of Water-Gas Shift and Methanol Reforming on Pt/Al_2O_3 Catalysts in Vapor and Liquid Phases, J. Phys. Chem. B 109(7) (2005) 2810-2820

[10] Y. Guo, M.U. Azmat, X. Liu, Y. Wang, G. Lu, Effect of support's basic properties on hydrogen production in aqueous-phase reforming of glycerol and correlation between WGS and APR, Appl. Energ. 92 (2012) 218-223

[11] P.J. Dietrich, M.C. Akatay, F.G. Sollberger, E.A. Stach, J.T. Miller, W.N. Delgass, F.H. Ribeiro, Effect of Co Loading on the Activity and Selectivity of PtCo Aqueous Phase Reforming Catalysts, ACS Catal. 4(2) (2014) 480-491

[12] A. Morales-Marín, J.L. Ayastuy, U. Iriarte-Velasco, M.A. Gutiérrez-Ortiz, Nickel aluminate spinel-derived catalysts for the aqueous phase reforming of glycerol: Effect of reduction temperature, Appl. Catal. B:Environ. 244 (2019) 931-945

[13] A. Seretis, P. Tsiakaras, Crude bio-glycerol aqueous phase reforming and hydrogenolysis over commercial SiO_2-Al_2O_3 nickel catalyst, Renew. Energ. 97 (2016) 373-379

[14] L.I. Godina, A.V. Kirilin, A.V. Tokarev, I.L. Simakova, D.Y. Murzin, Sibunit-Supported Mono- and Bimetallic Catalysts Used in Aqueous-Phase Reforming of Xylitol, Ind. Eng. Chem. Res. 57(6) (2018) 2050-2067

[15] C. He, J. Zheng, K. Wang, H. Lin, J.Y. Wang, Y. Yang, Sorption enhanced aqueous phase reforming of glycerol for hydrogen production over Pt-Ni supported on multi-walled carbon nanotubes, Appl. Catal. B:Environ. 162 (2015) 401-411

[16] D. Li, Y. Li, X. Liu, Y. Guo, C.W. Pao, J.L. Chen, Y. Hu, Y. Wang, $NiAl_2O_4$ Spinel Supported Pt Catalysts: High Preformance and Origin in Aqueous-Phase Reforming of Methanol, ACS Catal. 9 (2019) 9671-9682

[17] L.A. Dosso, C.R. Vera, J.M. Grau, Aqueous phase reforming of polyols from glucose degradation by reaction over Pt/alumina catalysts modified by Ni or Co, Int. J. Hydrogen Energ. 42(30) (2017) 18853-18864

[18] M. El Doukkali, A. Iriondo, J.F. Cambra, P.L. Arias, Recent Improvement on H_2 Production by Liquid Phase Reforming of Glycerol: Catalytic Properties and Performance, and Deactivation Studies, Top. Catal. 57 (2014) 1066-1077

[19] A. Arandia, I. Coronado, A. Remiro, A.G. Gayubo, M. Reinikainen, Aqueous-phase reforming of bio-oil aqueous fraction over nickel-based catalysts, Int. J. Hydrogen Energ. 44(26) (2019) 13157-13168

[20] G. Wen, Y. Xu, H. Ma, Z. Xu, Z. Tian, Production of hydrogen by aqueous-phase reforming of glycerol, Int. J. Hydrogen Energ. 33(22) (2008) 6657-6666

[21] J. Zhang, W. Yan, Z. An, H. Song, J. He, Interface-Promoted Dehydrogenation and Water-Gas Shift toward High-Efficient H_2 Production from Aqueous Phase Reforming of Cellulose, ACS Sustainable Chem. Eng. 6(6) (2018) 7313-7324

[22] F. Cai, D. Pan, J.J. Ibrahim, J. Zhang, G. Xiao, Hydrogenolysis of glycerol over supported bimetallic Ni/Cu catalysts with and without external hydrogen addition in a fixed-bed flow reactor, Appl. Catal. A:Gen. 564 (2018) 172-182

[23] J.O. Maloney, Perry's handbook of chemical engineering, eighth ed., McGraw-Hill Companies, Inc., 2008

[24] J.H. Kwak, J.Z. Hu, D.H. Kim, J. Szanyi, C.H.F. Peden, Penta-coordinated Al^{3+} ions as preferential nucleation sites for BaO on γ-Al_2O_3: An ultra-high-magnetic field ^{27}Al MAS NMR study, J. Catal. 251(1) (2007) 189-194

[25] M. Jabłońska, TPR study and catalytic performance of noble metals modified Al_2O_3, TiO_2 and ZrO_2 for low-temperature NH_3-SCO, Catal. Commun. 70 (2015) 66-71

[26] E.V. Benvenutti, L. Franken, C.C. Moro, C.U. Davanzo, FTIR Study of Hydrogen and Carbon Monoxide Adsorption on Pt/TiO_2, Pt/ZrO_2, and Pt/Al_2O_3, Langmuir 15 (1999) 8140-8146

[27] J.M. Zhang, S.N. Sun, Y. Li, X.J. Zhang, P.Y. Zhang, Y.J. Fan, A strategy in deep eutectic solvents for carbon nanotube-supported PtCo nanocatalysts with enhanced performance toward methanol electrooxidation, Int. J. Hydrogen Energ. 42(43) (2017) 26744-26751

[28] J.Z. Shyu, K. Otto, Identification of platinum phases on γ-alumina by XPS, Appl. Surf. Sci. 32(1-2) (1988) 246-252

[29] S. Kannan, C.S. Swamy, Catalytic decomposition of nitrous oxide over calcined cobalt aluminum hydrotalcites, Catal. Today 53(4) (1999) 725-737

[30] A. Iriondo, J.F. Cambra, V.L. Barrio, M.B. Guemez, P.L. Arias, M.C. Sanchez-Sanchez, R.M. Navarro, J.L.G. Fierro, Appl. Catal. B:Environ. 106(1-2) (2011) 83-93

[31] I. Coronado, M. Stekrova, M. Reinikainen, P. Simell, L. Lefferts, J. Lehtonen, A review of catalytic aqueous-phase reforming of oxygenated hydrocarbons derived from biorefinery water fractions, Int. J. Hydrogen Energ. 41(26) (2016) 11003-11032

[32] N. Tsubaki, S. Sun, K. Fujimoto, Different Functions of the Noble Metals Added to Cobalt Catalysts for Fischer-Tropsch Synthesis, J. Catal. 199 (2001) 236-246

[33] A. Wawrzetz, B. Peng, A. Hrabar, A. Jentys, A.A. Lemonidou, J.A. Lercher, Towards understanding the bifunctional hydrodeoxygenation and aqueous phase reforming of glycerol, J. Catal. 269(2) (2010) 411-420

[34] J. So, Y. Chung, D.S. Sholl, C. Sievers, In-situ ATR-IR study of surface reaction during aqueous phase reforming of glycerol, sorbitol and glucose over Pt/γ-Al_2O_3, Molec. Catal. 475 (2019) 110423

[35] I.D. González, R.M. Navarro, W. Wen, N. Marinkovic, J.A. Rodriguez, F. Rosa, J.L.G. Fierro, A comparative study of the water gas shift reaction over platinum catalysts supported on CeO_2, TiO_2 and Ce-modified TiO_2, Catal. Today 149(3-4) (2010) 372-379

[36] J.P. Clay, J.P. Greeley, F.H. Ribeiro, W.N. Delgass, W.F. Schneider, DFT comparison of intrinsic WGS kinetics over Pd and Pt, J. Catal. 320 (2014) 106-117

[37] P.J. Dietrich, F.G. Sollberger, M.C. Akatay, E.A. Stach, W.N. Delgass, J.T. Miller, F.H. Ribeiro, Structural and catalytic differences in the effect of Co and Mo as promoters for Pt-based aqueous phase reforming catalysts, Appl. Catal. B:Environ. 156-157 (2014) 236-248

[38] R.M. Ravenelle, J.R. Copeland, W.G. Kim, J.C. Crittenden, C. Sievers, Structural Changes of γ-Al$_2$O$_3$-Supported Catalysts in Hot Liquid Water, ACS Catal. 1 (2011) 552-561

[39] T. van Haasterecht, C.C.I. Ludding, K.P. de Jong, J.H. Bitter, Stability and activity of carbon nanofiber-supported catalysts in the aqueous phase reforming of ethylene glycol, J. Energy Chem. 22(2) (2013) 257-269

[40] C. Sievers, Y. Noda, L. Qi, E.M. Albuquerque, R.M. Rioux, S.L. Scott, Phenomena Affecting Catalytic Reactions at Solid-Liquid Interfaces, ACS Catal. 6(12) (2016) 8286-8307

[41] D.J.M. de Vlieger, D.B. Thakur, L. Lefferts, K. Seshan, Carbon Nanotubes: A Promising Catalyst Support Material for Supercritical Water Gasification of Biomass Waste, ChemCatChem 4(12) (2012) 2068-2074

[42] W. Yu, M.D. Porosoff, J.G. Chen, Review of Pt-Based Bimetallic Catalysis: From Model Surfaces to Supported Catalysts, Chem. Rev. 112(11) (2012) 5780-5817

[43] W. Chen, T.F. Kimpel, Y. Song, F.K. Chiang, B. Zijlstra, R. Pestman, P. Wang, E.J.M. Hensen, Influence of Carbon Deposits on the Cobalt-Catalyzed Fischer-Tropsch Reaction: Evidence of a Two-Site Reaction Model, ACS Catal. 8(2) (2018) 1580–1590

[44] V. Klouz, V. Fierro, P. Denton, H. Katz, J.P. Lisse, S. Bouvot-Mauduit, C. Mirodatos, Ethanol reforming for hydrogen production in a hybrid electric vehicle: process optimisation, J. Power Sources 105(1) (2002) 26-34

Supporting Information

Highly stable Pt/CoAl₂O₄ catalysts in Aqueous-Phase Reforming of glycerol

A.J. Reynoso [a], U. Iriarte-Velasco [b], M.A. Gutiérrez-Ortiz [a], J.L. Ayastuy [a, *]

[a]   A.J. Reynoso, M.A. Gutiérrez-Ortiz, J.L. Ayastuy

Chemical Technologies for the Environmental Sustainability Group

Department of Chemical Engineering, Faculty of Science and Technology

University of the Basque Country UPV/EHU, Sarriena S/N, 48940 Leioa, Spain

Corresponding author: joseluis.ayastuy@ehu.eus

[b]   U. Iriarte-Velasco

Chemical Technologies for the Environmental Sustainability Group

Department of Chemical Engineering, Faculty of Pharmacy

University of the Basque Country UPV/EHU,

Paseo de la Universidad, 7, 01006 Vitoria, Spain

1.1 Calibration of gas and liquid compounds

Gas compound	R^2	Equipment
Helium	0.999959	µGC (channel 1)
Hydrogen	0.997904	µGC (channel 1)
Nitrogen	0.998172	µGC (channel 2)
Methane	0.997753	µGC (channel 2)
Carbon monoxide	0.999399	µGC (channel 2)
Carbon dioxide	0.998006	µGC (channel 3)
Ethylene	0.998277	µGC (channel 3)
Ethane	0.999624	µGC (channel 3)
Propane	0.955711	µGC (channel 4)
Propylene	0.995271	µGC (channel 4)
n-Butane	0.998724	µGC (channel 4)

Channel 1: column (Molecular sieve (MS5A HI), carrier Ar
Channel 2: column (Molecular sieve (MS5A HI)), carrier He
Channel 3: column (Poraplot (PPQ)), carrier He
Channel 4: column (Al_2O_3-KCl), carrier He

Liquid compound	R^2	Equipment
Glycerol	0.9985	HPLC
1-Propanol	0.9961	GC-FID
2-Propanol	0.9895	GC-FID
Acetaldehyde	0.9872	GC-FID
Acetic acid	0.9928	GC-FID
Acetone	0.9999	GC-FID
Ethanol	0.9995	GC-FID
Ethylene glycol	0.9990	GC-FID
Hydroxyacetone	0.9997	GC-FID
Methanol	0.9998	GC-FID
Propionic acid	0.9935	GC-FID
Propylene glycol	0.9978	GC-FID

HPLC: column (Hi-Plex H)
GC-FID: column (HP-WAX), carrier He

1.2 XPS spectra for Al 2p and Pt 4d5/2 in reduced samples

(A)

Al (2p)

CoAl

0.3Pt/CoAl

1Pt/CoAl

0.3Pt/Al

82 80 78 76 74 72 70 68 66

BE (eV)

(B)

Pt 4d$_{5/2}$

0.3Pt/CoAl
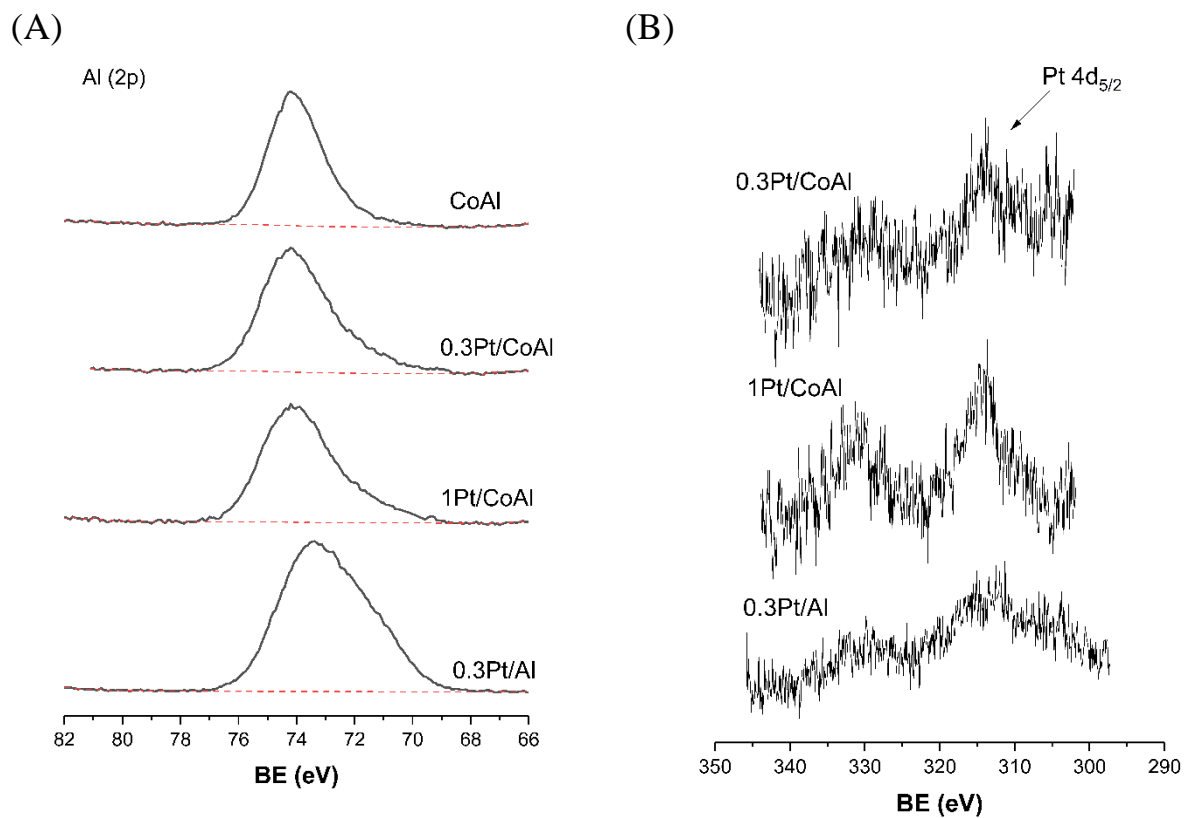
1Pt/CoAl

0.3Pt/Al

350 340 330 320 310 300 290

BE (eV)

Figure S1. XPS spectrum of Al 2p (A) and Pt 4d5/2 (B) in the reduced samples.

1.3 TOS evolution of gas products and liquid products.
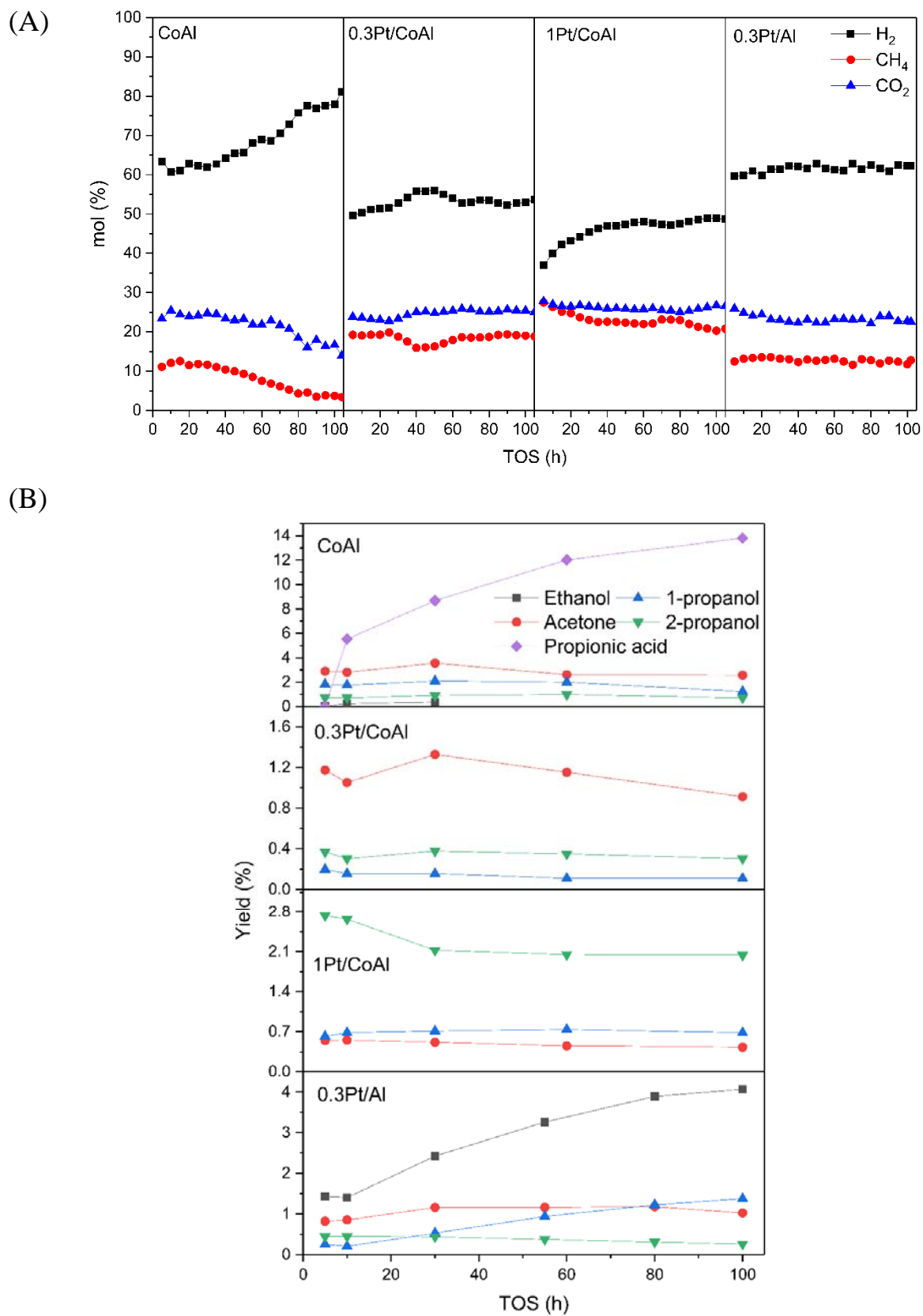
(A)

(B)

Figure S2. Evolution with TOS of (A) main compounds of the gas phase and (B) liquid products yield. Reaction conditions: 260 ºC/50 bar, 10 wt.% glycerol, WHSV=0.68 h^{-1}